

A Mach number study of the Richtmyer–Meshkov instability in a varicose, heavy-gas curtain

G. C. Orlicz,^{a)} B. J. Balakumar, C. D. Tomkins, and K. P. Prestridge
 Los Alamos National Laboratory, Los Alamos, New Mexico 87545, USA

(Received 15 October 2008; accepted 7 April 2009; published online 4 June 2009)

A varicose-perturbed, thin, heavy-gas curtain is impulsively accelerated by a planar shock wave of varying strength and investigated experimentally using concentration field visualization. Experiments were performed with Mach 1.2 and 1.5 incident shock waves, acquiring images of the initial conditions, and 18 different times after shock interaction in each case. Repeatability of the initial conditions allows for visualization of flow feature development over time for both Mach numbers despite capturing only one dynamic, postshock image per run of the experiment. Good agreement between integral width experimental data and a mixing width model is demonstrated for early to intermediate times in the flow. Integral width growth rates for Mach 1.2 and 1.5 are shown to collapse using a scaling based upon the convection velocity of the curtain. The diffusion driven instantaneous mixing rate, χ , is also estimated and compared between experiments. Results from this gradient based metric show differences in mixing trends between Mach numbers that do not scale in the same way as integral width, suggesting that integral width alone is insufficient for completely describing the flow. An experiment with a Mach 2.0 incident shock was carried out for the first time in the experimental facility. The resulting image provides further evidence for the mixing trends observed in this paper as Mach number is increased. © 2009 American Institute of Physics. [DOI: 10.1063/1.3147929]

I. INTRODUCTION

The instability arising at the interface between two fluids of different densities due to the misalignment of pressure and density gradients under an impulsive acceleration is known as the Richtmyer–Meshkov (RM) instability.^{1,2} It is a limiting case of the Rayleigh–Taylor (RT) instability^{3,4} that occurs when a constant acceleration, such as gravity, acts in the direction from a heavy fluid to a light fluid. Any perturbation that exists at the interface will grow with time, yielding complex nonlinear solutions with even the most simple initial conditions [e.g., a two-dimensional (2D) sinusoid], eventually mixing the two fluids. In the RM case, the interface becomes unstable regardless of the direction (i.e., heavy to light or light to heavy) of the impulsive acceleration (e.g., shock wave).⁵ This makes the focus of the current study, a double interface created by a heavy-fluid layer, a problem rich in physics.

While the RM instability provides insight into aspects of fundamental fluid mechanics, it also occurs in engineering applications and astrophysical phenomena encompassing a wide range of scales. Common examples include inertial confinement fusion,⁶ supersonic combustion ramjet engines,⁷ deflagration-to-detonation transition,⁸ and supernovas.⁹

The underlying mechanism for the amplification of initial perturbations in the RM instability is baroclinic vorticity deposition, generated by the misalignment of pressure (shock wave) and density gradients (fluid interface).⁵ In the simplest case of a 2D sinuous interface with small initial perturbation amplitude, vorticity amplifies the perturbations, causing the

peaks and troughs of the interface to grow linearly in time. As time progresses, the peaks and troughs grow asymmetrically, with spikes of heavy fluid penetrating into light fluid, and bubbles of light fluid penetrating into heavy fluid.⁵ When the perturbation amplitude approaches that of the wavelength, the growth is nonlinear. At later times, vorticity causes the spikes to evolve, rolling up into mushroom shaped structures, and both the Kelvin–Helmholtz shear instability and the RT instability due to centrifugal forces cause small scale features to appear along the distorting interface.⁵ Eventually, this may lead to turbulent mixing.

While single interface experiments are desirable test cases for the validation of models, other more complex interfacial configurations have also been studied. These include spherical soap film bubbles of light or heavy gas in vertical shock tubes,^{10–12} laminar jet cylinders of light or heavy gas,^{13–15} and heavy gas curtains with membranes¹⁶ and membraneless curtains^{17–25} in horizontal shock tubes. Another experiment compared the RM instability resulting from five different configurations of SF₆ cylinders.²⁶

In the present study, the interface of interest is a thin, membraneless, varicose, heavy-gas (SF₆) curtain flowing in air. This configuration is sometimes referred to as *A-B-A*, in the sense that one fluid, *B*, is sandwiched by fluid *A*, creating two nearby interfaces. The existence of two adjacent interfaces adds a level of complexity to the dynamics of the RM instability, as the initial perturbations on either side of the curtain do not grow independently, but interact and influence each other's development. It is because of this interaction that we characterize this configuration as “thin.” Studying configurations with two or more interfaces may be valuable

^{a)}Electronic mail: orlicz@lanl.gov.

for understanding mixing in supernovas, where the expanding shock wave passes through several layers of stratified gas, or in cryogenic deuterium-tritium (DT) capsules for inertial confinement fusion, where a shell/DT ice interface is impulsively driven before the converging shock accelerates the DT ice/DT gas interface.^{27,28} The curtain is formed using a similar approach as in the laminar heavy gas jet cylinder experiments,^{13–15,26} and the cross-sectional shape of the curtain relies upon the shape of the nozzle. In both the flowing cylinder and curtain experiments, a small amount of diffusion occurs prior to shock impact, resulting in a diffuse interface of finite thickness.

Two significant obstacles for the experimental study of the RM instability are (1) the creation of a well-characterized and repeatable fluid interface, and (2) the implementation of adequate diagnostics. The first obstacle has been a major stumbling block for previous gas curtain studies. In the first varicose curtain experiments, three distinct flow morphologies were reported from the same nominal initial conditions.¹⁷ Later these morphologies were observed experimentally and shown numerically to be the result of small differences in the initial conditions,^{18,29} highlighting the sensitivity of the resulting RM instability to even very small changes in initial conditions. Moreover, it emphasized the importance of being able to generate repeatable initial conditions with good characterization. Through the use of a specially designed nozzle,^{25,30} the initial conditions in the present study are the most repeatable for any gas curtain to date. To overcome the second obstacle, the use of high resolution planar laser induced fluorescence (PLIF) allows for qualitative and quantitative interrogation of mechanisms that drive the resulting RM instability.

The goal of the present study is to investigate the effects on the development of the RM instability and subsequent fluid mixing when the incident shock wave Mach number is varied within the weak shock regime ($M \leq 2$). The highly repeatable nature of the initial conditions permits isolation of Mach number effects in the present work.

Previous reports studying Mach number effects in the RM instability are sparse. A Mach number experiment by Jacobs and Krivets³¹ studies the instability growth on a membraneless single interface between air and SF₆ with incident shocks of $M=1.1, 1.2,$ and 1.3 . The experiments showed that the amplitude growth for the Mach numbers studied could be collapsed if time is nondimensionally scaled using Richtmyer's linear formula.

Two separate experiments carried out by Ranjan *et al.*¹⁰ discuss results of increasing Mach number for a spherical heavy argon bubble, and a spherical light helium bubble,¹¹ both in atmospheric nitrogen. In both cases, high Mach number incident shock waves ($M \geq 2.88$) resulted in flow features that were not previously observed in lower Mach number experiments. The researchers attribute these features to differences in compressibility effects, and to more complex shock refraction and reflection phenomena occurring with stronger incident shocks.

In solid-solid sinusoidal interface Nova laser experiments by Holmes *et al.*,³² with incident shock Mach numbers of 10.8 and 15.3, it was found that absolute perturbation

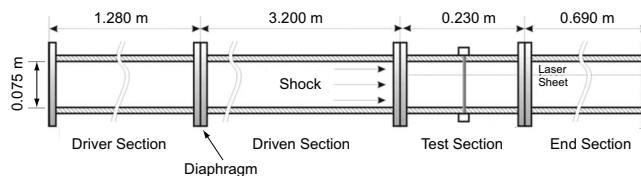


FIG. 1. Shock tube schematic (Ref. 15), with a 75×75 mm² square cross section.

growth rate increases with Mach number. However, the growth rates relative to those predicted by Richtmyer's linear formulation reduce with increasing Mach number. This is attributed to higher compression of the geometric perturbations at the interface, and resulting changes in the postshock Atwood numbers as Mach number is increased. Atwood number is defined as $A = (\rho_2 - \rho_1) / (\rho_2 + \rho_1)$, where ρ is the fluid density, and by convention, the acceleration is directed from fluid 2 to fluid 1.

The current study presents a comprehensive investigation of experiments carried out at two Mach numbers for the first time in a varicose, membraneless, heavy-gas curtain, yielding differences in complex flow features at multiple scales. The imaging technique allows for the quantitative analysis of integral mixing width growth and instantaneous mixing rate, as well as qualitative comparison of flow morphology between the different Mach number experiments.

II. EXPERIMENTAL SETUP

A side view schematic of the shock tube is shown in Fig. 1.¹⁵ The shock tube has a 75×75 mm² square cross section with a total length of approximately 5.4 m. The end section is open to the atmosphere. To create the shock wave, a polypropylene diaphragm is first placed in between the driver and driven sections. Then, compressed gas is flowed into the driver section until the desired pressure is reached (the required gauge pressure was experimentally determined to be ~ 0.103 MPa for Mach 1.2, ~ 0.345 MPa for Mach 1.5, and ~ 1.034 MPa for Mach 2.0). A signal is then sent to cause a solenoid-driven set of razor blades to rupture the diaphragm, thus releasing the pressure and causing a planar shock wave to form shortly downstream of the diaphragm location. As the shock wave moves downstream toward the initial conditions, four separate pressure transducers measure shock location, speed, and time of impact with initial conditions, as well as trigger the imaging diagnostics.

A. Initial conditions

The initial condition in the present study is a thin, varicose, sulfur hexafluoride (SF₆) gas curtain. To create the initial condition, a settling chamber located above the test section is filled with SF₆. Before the shock wave is released, a valve is opened to allow a gravity driven flow of SF₆ from the settling chamber through the nozzle and into the test section (Fig. 2). Porous, flow straightening foam is also placed just before the nozzle to help ensure laminar flow. The nozzle itself consists of a single row of closely spaced holes of $S/D=1.2$, where the spacing, S , is 3.6 mm, and the

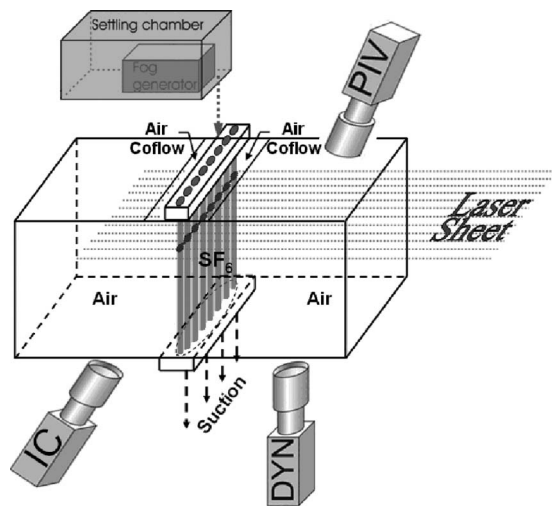


FIG. 2. Test section schematic showing initial conditions and coflow. When fired, the shock wave will move from left to right.

diameter, D , is 3.0 mm. Inlets on either side of the nozzle allow air to be passively entrained into the shock tube, stabilizing the initial conditions and enhancing experimental reproducibility.^{25,30} As the SF_6 flows out of the nozzle and into the test section (see photograph taken from the end of the runout section in Fig. 3), diffusion of the SF_6 cylinders creates a varicose perturbed SF_6 curtain in the surrounding air. At the bottom of the test section, a mild, variable suction exhausts the SF_6 out of the shock tube. The vertical flow velocity (~ 0.1 m/s) can be neglected as it is small compared to the horizontal velocity of the shock-induced flow (>97 m/s). Characterization of the initial conditions can be found in Balakumar *et al.*²⁵ Although the peak concentration of the initial conditions in the present study may be different, this characterization should be useful for initialization of numerical simulations for comparison with the experimental data.

B. Imaging diagnostics

The initial condition and the dynamic flow evolution after shock passage are visualized using PLIF with acetone vapor as the tracer. To obtain the acetone vapor seeding, SF_6 is bubbled through liquid acetone in a 20 °C bath. For visualization, a neodymium-doped yttrium aluminum garnet frequency quadrupled pulsed laser is formed into a thin sheet (<1 mm). The laser output peaks at 266 nm (ultraviolet), providing about 12 mJ/pulse with a pulse width of about 10 ns. The ultraviolet (UV) light sheet causes the acetone tracer to fluoresce between 350 and 550 nm with a peak at ~ 400 nm. The acetone vapor molecularly mixes with the SF_6 , giving rise to high-resolution, two-dimensional images representative of SF_6 concentration.

The horizontal laser sheet enters the shock tube through an UV-transparent window at the end of the end section, as seen in Fig. 1, and is positioned to visualize cross sections of the curtain located 2 cm below the nozzle exit. For each experiment, two PLIF images are obtained. In general, one pulse is used for illuminating the initial conditions about



FIG. 3. Photograph of the axis view of the shock tube (looking through the window at the end of the end section) showing the varicose curtain initial conditions flowing from top to bottom. Visualization using fog droplets for flow seeding in the SF_6 and a flashlight for illumination.

$5 \mu\text{s}$ before shock impact, and the other pulse captures a postshock dynamic image of the flow at a specified time.

The images are captured using two separate, cooled, back-illuminated Apogee charge-coupled device (CCD) cameras. The camera that captures the fluorescence from the initial condition pulse, labeled “IC” in Fig. 2, has a 14 bit, 2184×1470 CCD array, but is 3×3 binned on the chip to increase signal-to-noise ratio, yielding a 728×490 pixels image. The IC camera is also slightly tilted as shown in Fig. 2 to gain optical access to the initial conditions. The IC images are corrected for distortion using calibration images of a square grid. The 16 bit dynamic camera, labeled “DYN” in Fig. 2, is oriented orthogonally to the plane of the laser sheet, and has an unbinned 1024×1024 CCD. Both the IC and the dynamic camera provide high resolution images: 52 and $54 \mu\text{m}/\text{pixel}$, respectively. A set of background images are also captured every 15 experimental runs, and are subtracted from each experimental image, compensating for both ambient light variation, and temperature effects on the CCD chips. The processed images give the intensity of fluorescence from the acetone vapor, which scales linearly to SF_6 concentration, yielding 2D SF_6 concentration maps.

C. Mach number variability

In the present study, the Mach number is varied by using helium as the driver gas and changing the driver pressure. When helium is used as the driver gas, theoretical calculations show that the expansion fan from the opposite end of the shock tube arrives at the test section at $t=945 \mu\text{s}$ and $t=740 \mu\text{s}$ for Mach 1.2 and 1.5, respectively. By these times, the interface has moved past the test section field of view. Also, there was no experimental evidence of interaction of the expansion fan with the evolving curtain, as the curtain’s convection velocity remained steady, and no dramatic change in the flow evolution was observed. Figure 4 is a position versus time diagram showing the shock dynamics for a $M=1.2$ experiment, generated using a one-dimensional (1D) code developed at the University of Wisconsin and altered to the specifications of the experimental conditions in the current study. As shown in Fig. 4, the locations of the

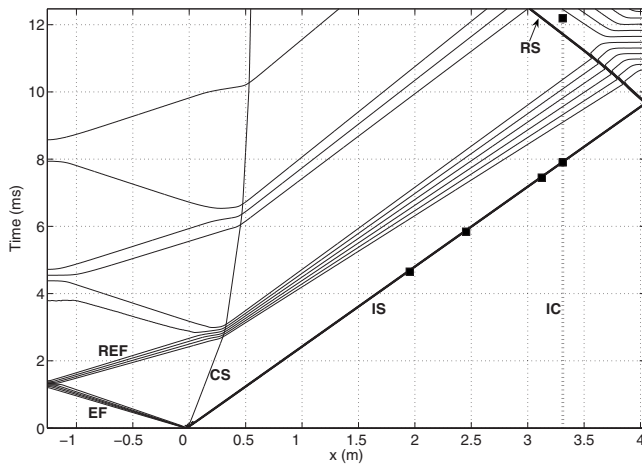


FIG. 4. Theoretical $x(m)-t(ms)$ wave diagram, where x is the location along the shock tube and t is the time, for Mach 1.2 with experimental pressure trace rises overlaid (squares). $x=0$ is the location of the diaphragm. IS, incident shock; RS, reflected shock; EF, expansion fan; REF, reflected expansion fan; CS, contact surface; IC, location of initial conditions.

shock wave as experimentally measured from the rise in signal from the pressure transducers agree very well with the predicted incident shock speed.

III. RESULTS

In general, experiments were performed to capture several images at each time investigated. Time sequenced images were compiled from this data to visualize the evolution of the gas curtain for experiments at Mach 1.2 (420 m/s relative to ground) and Mach 1.5 (532 m/s) incident shocks. One run of the experiment was also performed at Mach 2.0 (692 m/s), measuring the density field at a single time after shock impact. In both Mach 1.2 and 1.5 experiments, the timing of the dynamic PLIF pulse was varied from just after shock impact to as late in time as could be imaged within the test section. Also, in both data sets, some early time dynamic images were captured with the IC camera, as its field of view included a region 12 mm downstream of the initial condition location. Initial conditions were not captured when acquiring these early time dynamic images.

In order to help ensure that the initial conditions remained nominally identical, experiments were performed periodically with timings and incident shock Mach numbers that matched those taken earlier. These dynamic validation images and the initial condition images were both used to determine the repeatability of the experiment.

Using the data collected in both Mach 1.2 and 1.5 experiments, the streamwise location of the center of mass against time was calculated and is plotted in Fig. 5. The streamwise center of mass of the curtain within an image was measured by spanwise-averaging intensity over a region of the image chosen to include several wavelengths of the curtain. The average, intensity-weighted pixel position within the resulting 1D streamwise function was then defined to be the streamwise center of mass within the image. Best fit lines to the data accumulated by the dynamic camera (DYN) were obtained, giving average convective velocities of 97.4 m/s

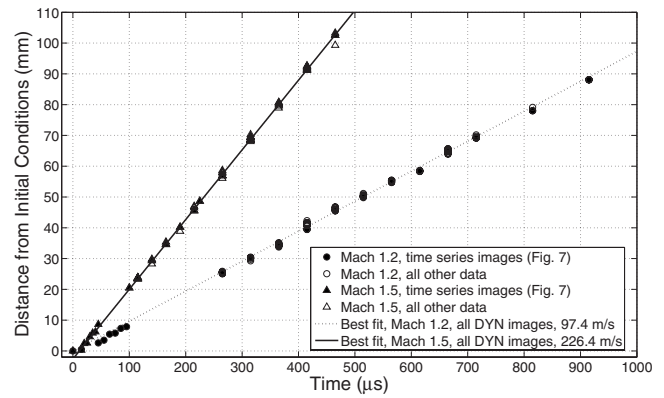


FIG. 5. Downstream location of center of mass vs time. Linear best fits do not include data points from the IC camera. Based on fits, average convection velocities are 97.4 and 226.4 m/s for Mach 1.2 and 1.5, respectively.

for Mach 1.2, and 226.4 m/s for Mach 1.5. As can be seen in Fig. 5, the data points all fall very closely onto the best fit lines with little scatter, showing that the convection velocity is constant throughout the experiment despite the generation of vorticity from mechanisms after shock passage. It also indicates that the expansion fan does not reach the test section at any time throughout the duration of the experiment. The small amount of scatter in the data is due to small variations in the shock speed between experiments.

A. Flow morphology observations

The flow morphology in the current study is dominated by pairs of closely spaced, interacting vortices generated through baroclinic vorticity deposition. The distortion of the fluid interfaces gives rise to complex flow features that are highly dependent upon the initial conditions. Figure 6 defines the flow features seen in the experiments.

The flow evolution can be seen in Fig. 7, where a time series for both the Mach 1.2 and the Mach 1.5 data sets is compiled. Each image in the time series corresponds to a separate experiment, and due to small differences in the initial conditions, small scale features do not always register

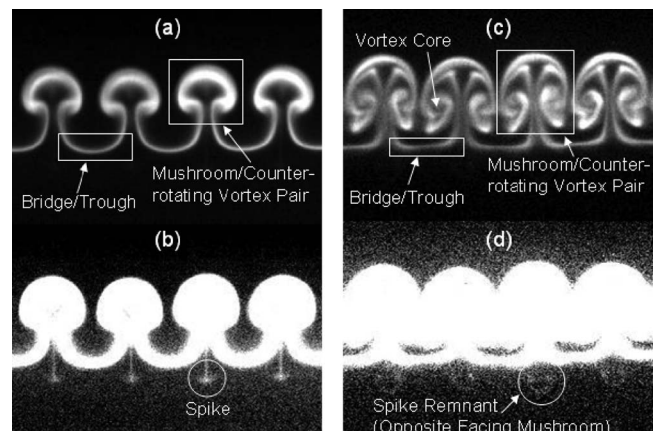


FIG. 6. Flow feature nomenclature: Left: (a) A Mach 1.5 shot at 115 μs . (b) The same image with contrast adjusted to visualize the spike flow feature; Right: (c) A Mach 1.5 shot at 215 μs , (d) The same image with contrast adjusted to view remnants of spike roll up.

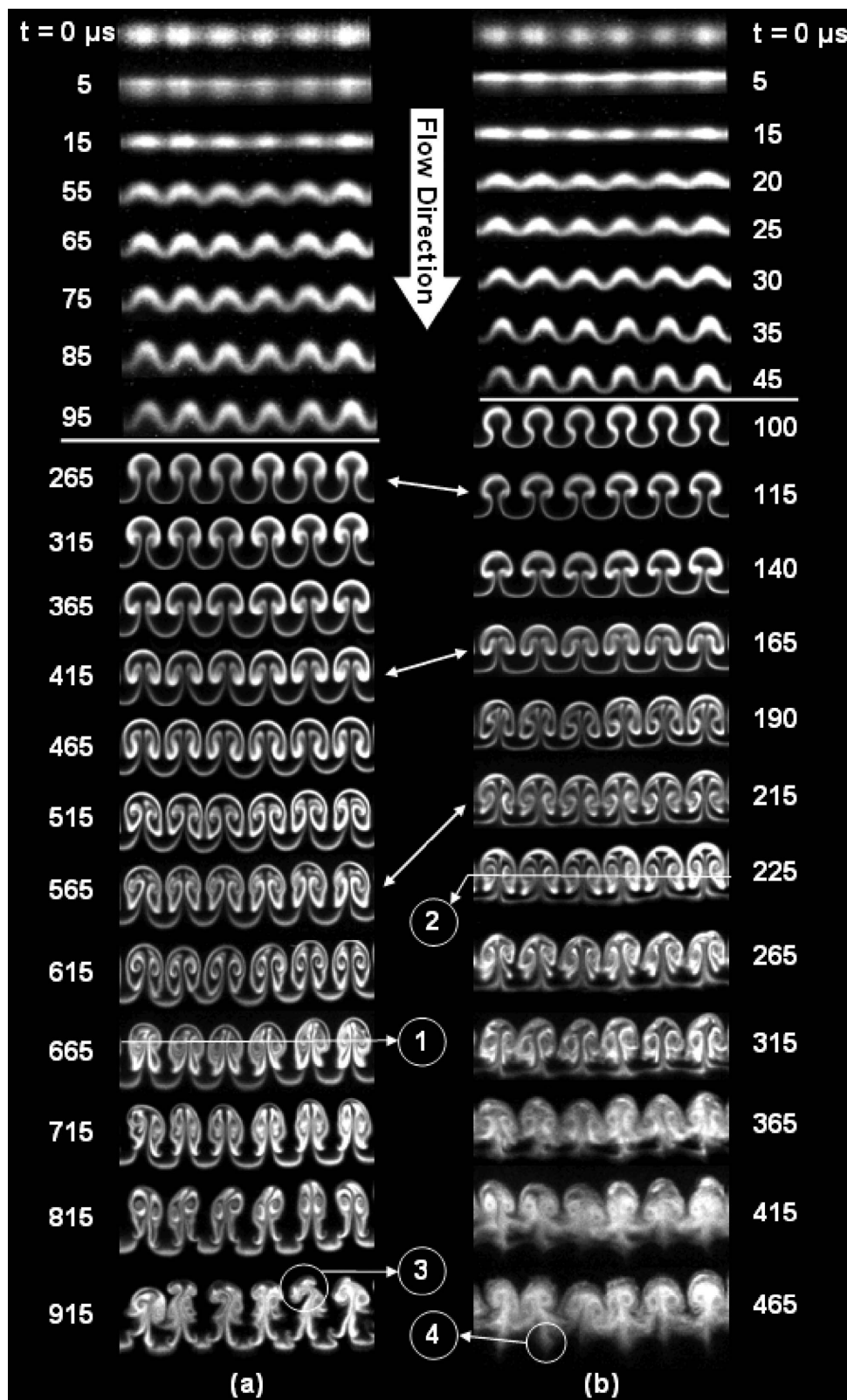


FIG. 7. Time series for (a) Mach 1.2, and (b) Mach 1.5, with times in μs . White indicates SF_6 , while black indicates air. ICs correspond to $t=0 \mu\text{s}$; shock compression corresponds to $15 \mu\text{s}$. Flow is from top to bottom. The spanwise extent of the structures in each image is 22 mm. Lines separating the data show the camera transition from IC to DYN in each data set. Double headed arrows show time comparisons in terms of degree of flow development. 1 and 2 show the average streamwise location of the vortex cores in images for Mach 1.2 and 1.5, respectively, as is discussed in the text. 3 indicates the development of secondary vortex cores, and 4, the protruding bridge material, as is discussed in the text.

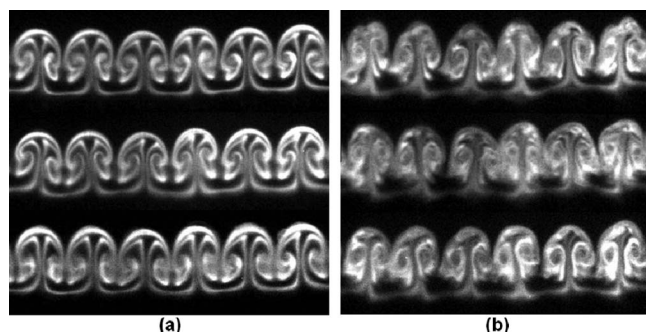


FIG. 8. Illustration of repeatability: (a) three images at $215 \mu\text{s}$ after shock impact corresponding to individual runs of the Mach 1.5 experiment; (b) three images at $315 \mu\text{s}$ after shock impact corresponding to individual runs of the Mach 1.5 experiment.

from frame to frame. However, the highly repeatable nature of the dynamic images in the present study suggests that the initial conditions were more repeatable than those for any previously reported thin, heavy-gas curtain. This permits the tracking of large scale features and some small scale features through their development in time. Figure 8 shows two sets of three images at times of $t=215 \mu\text{s}$ and $t=315 \mu\text{s}$ from different runs of the Mach 1.5 experiment, and demonstrates the remarkable repeatability of the current study even at later times when mixing in the vortex cores is occurring, and flow complexity is high. The data sets used to generate the time series comprise several images at most times. The images for the time series in Fig. 7 were selected based on qualitative registering of flow features, and spanwise symmetry within the individual image.

As seen in Fig. 7, the ICs are captured just before shock impact ($t=0 \mu\text{s}$). At $t=5 \mu\text{s}$, the shock wave is imaged as it travels through the ICs, eventually compressing the curtain at $t=15 \mu\text{s}$. After the compression phase has occurred, the perturbations on the upstream edge begin to grow while a phase inversion takes place on the downstream edge. This is evident in the image at $t=55 \mu\text{s}$ for Mach 1.2 and $t=20 \mu\text{s}$ for Mach 1.5. The subsequent flow morphology for Mach 1.2 and 1.5 is fairly similar on large scales at early times (before vortex cores have formed) to intermediate times (when vortex cores have formed until $t=715 \mu\text{s}$ for Mach 1.2, and $t=265 \mu\text{s}$ for Mach 1.5). See Fig. 6 for an example of a vortex core. The growth of the initial perturbations occurs faster in Mach 1.5 experiments due to the greater amount of vorticity deposited on the interfaces by the shock wave. At various times, indicated by double headed arrows in Fig. 7, many flow features are qualitatively similar, including the amount of main vortex roll up and the degree of fluid mixing. The differences in time between each of these comparisons ($\Delta t=150 \mu\text{s}$ for Mach 1.2, and $\Delta t=50 \mu\text{s}$ for Mach 1.5) suggest that the large scale flow morphology develops approximately three times faster in the Mach 1.5 experiment.

Subtle differences do exist at early to intermediate times, such as the average streamwise location of the main vortex cores, indicated by labels 1 and 2 in Fig. 7, with respect to the location of the streamwise center of mass. In the Mach 1.2 image, the vortex cores (identified visually) are located on average 0.68 mm upstream of the streamwise location of

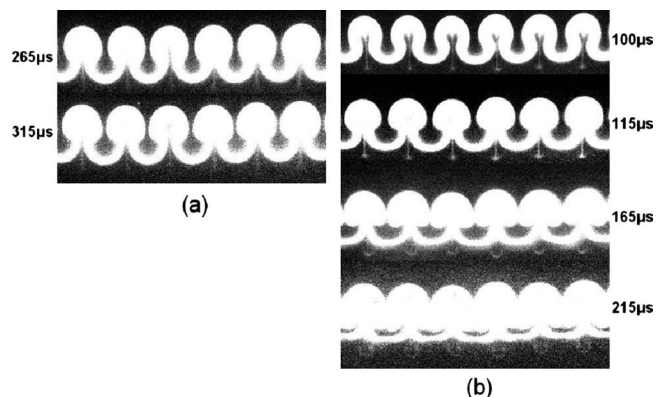


FIG. 9. Contrast adjusted images showing the evolution of the spike structure over time for (a) Mach 1.2 and (b) Mach 1.5 experiments.

the spanwise-averaged center of mass, while in the Mach 1.5 image, the average location of the vortex cores is only 0.16 mm upstream. Also, in the Mach 1.2 flow morphology, the bridges stretch farther away from the main structure and are more rounded than in the Mach 1.5 morphology.

At late times ($t \geq 715 \mu\text{s}$ for Mach 1.2, and $t \geq 265 \mu\text{s}$ for Mach 1.5), differences in the flow morphology become more prominent. In general, in the Mach 1.2 flow, the individual vortex pairs (mushrooms) remain more widely spaced throughout their growth, and become more elongated, while the Mach 1.5 vortex pairs appear to grow more in the spanwise direction.

Also, differences in the relative streamwise position of vortex cores persist. Streamwise position was measured for each image in which vortices were clearly defined, and at each stage of development (in terms of large scale flow features and degree of roll up), the vortex cores are located farther upstream relative to the streamwise center of mass in the Mach 1.2 experiments. On average, the convective velocities for the vortex cores were determined to be 93.2 and 223.6 m/s for Mach 1.2 and 1.5 experiments, respectively. This corresponds to 96% (Mach 1.2) and 99% (Mach 1.5) of the center of mass convection velocity.

This difference in relative vortex core velocity between experiments can be explained by the difference in associated vortex strength. The stronger vortices in the Mach 1.5 experiments cause more material (SF_6) to be entrained into the main vortex. Therefore, more material, and thus the center of mass, lies closer to the location of the vortex cores. This is highlighted in Mach 1.5 experiments when observing that even the bridge material is drawn toward the spanwise center of the counter-rotating vortex pairs, gathering just downstream of the vortex pairs (see images from 265 to $365 \mu\text{s}$ in the Mach 1.5 case). Eventually, the bridge material from either side meets at the spanwise center, and is caused to protrude downstream (label 4 in Fig. 7). In the Mach 1.2 experiments the bridge material remains much less affected by the vortex cores. Instead, at late times, the vortices appear to “pinch” off, resulting in an apparent redistribution of vorticity (label 3).

Also, the Mach 1.5 case becomes more mixed at much earlier times. For example, based upon visual inspection, one

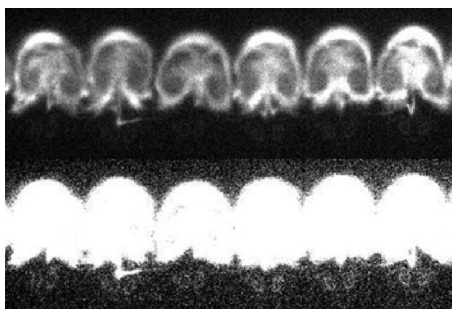


FIG. 10. Above: A Mach 2.0 shot at $185 \mu\text{s}$ after shock impact. Below: the same image with contrast adjustment to visualize spike roll up.

could determine that the degree of mixing that has occurred in the Mach 1.5 experiment by $t=315 \mu\text{s}$ or $365 \mu\text{s}$, has not occurred until the latest time, $t=915 \mu\text{s}$, for Mach 1.2.

Another Mach number effect observed in the current study is the amplitude of the spikes of material that are ejected downstream from the center of each mushroom structure at early times, circled in Fig. 6. As the refracted shock wave is focused on the downstream interface, a high localized pressure region causes a small amount of material to be ejected. This effect and its mechanism were first reported by Kumar *et al.*,²⁶ in which the shock focusing within an 8 mm heavy gas cylinder is clearly visualized in a Mach 1.2 experiment. The spike provides an example of a flow feature that appears to be generated on small scales, but grows to larger, resolved scales that are important for understanding material distribution throughout the mixing process. The existence of such features can provide a significant challenge for simulations.

Figure 9 shows contrast adjusted images that compare the evolution of the spike feature with time in experiments at Mach 1.2 and 1.5. Because the spike is formed from a small amount of material, the intensity of its PLIF signal is low, and it can be difficult to visualize without changing the contrast of the image as shown in Fig. 6. In the Mach 1.5 data, the higher associated pressure causes more mass to constitute the spike. With time, the spike itself is then observed to roll up into an opposite facing mushroom. As time increases, this material mixes with the surrounding air, thereby decreasing the PLIF signal until there is no evidence of the spike left at the latest times. In the Mach 1.2 experiments, remnants of the spike feature can only be seen in early time images (up to $t=415 \mu\text{s}$ in some cases), and there is no evidence of spike roll up. Additionally, one experiment was performed with a Mach 2.0 incident shock wave, and was imaged at $t=185 \mu\text{s}$ after shock impact (see Fig. 10). Evidence of opposite facing mushrooms (spike remnants) is observed in the contrast adjusted image, and they are significantly larger than those observed in the Mach 1.5 experiments. Over the range of Mach numbers studied, it appears that the higher the Mach number for the present set of initial conditions, the more material is ejected, and if applicable, the more prominent the opposite facing mushroom appears to be at later times.

It may be noted, that the initial conditions in the current study (a varicose gas curtain) are similar to those in the numerical study of Mikaelian²⁹ with a Mach 1.2 shock wave.

As can be seen in Fig. 10 of that study, the evolution of the instability is consistent with that of early time data in the present study. However, the instability evolves much faster in the current experimental set, and may be attributed to differences in initial conditions (the perturbation wavelength, λ , is 3.5 mm and 6.0 mm for experiment and simulation, respectively).

B. Integral widths

Two motivations for the present work are (1) to test the ability of a simple point-vortex model to capture the trends in integral width as a function of time, and (2) to determine the appropriate scaling of the integral width with Mach number. Integral width, defined as the distance spanning the farthest upstream and downstream location at which SF_6 is present within an individual image, represents the characteristic large scale of the flow and provides a first-order measure of mixing. Previous attempts to collapse integral width, or mixing width, for varying Mach numbers are based on the linear regime of the classic single interface problem (see, e.g., Refs. 31 and 33). The present configuration may be viewed as two closely spaced single interfaces that interact by interface coupling and feedthrough²⁹ because the interfacial perturbation amplitude grows to be comparable to the layer thickness, even at early times. It is an open question whether the mixing widths of thin shocked layers can also be effectively collapsed. Note that the growth of perturbations is expected to be nonlinear not only because of interfacial interaction but also because the amplitude, a , on both interfaces appears to quickly reach the same scale as the wavelength of the perturbations (i.e., $ka \approx 1$, where k is the wavenumber).

While many models exist for perturbation amplitude growth in single interface studies, their applicability is limited in the current dual-interface study. One model for the mixing width is applicable to the current study,¹⁹ however, and has shown good agreement with other varicose curtain experiments.^{20,23} The model is based upon an infinite row of counter-rotating point vortices, each with the same magnitude of circulation. The input parameters for the model include the circulation, Γ , the initial width just after shock compression, w'_0 (where ' denotes postshock conditions), and a single wave number, $k=2\pi/\lambda$, where λ is the wavelength of the perturbations. This model leads to a mixing width over time of

$$w(t) = \frac{2}{k} \sinh^{-1} \left[k^2 \Gamma (t - t_0) + \sinh \left(\frac{k w'_0}{2} \right) \right], \quad (1)$$

where t_0 is the time of the virtual origin of the width growth curve. The virtual origin was not included in the original model, but was added in order to account for the time taken for both the compression stage, and for phase inversion to occur on the downstream interface between SF_6 and air (where the shock wave is directed from heavy to light fluid).^{20,23} A list of parameter values can be found in Table I.

The integral width of the curtain was measured over one perturbation wavelength at the same spanwise location for each time, as shown in Fig. 11. The edge of the layer is taken

TABLE I. List of parameters governing the flow, including input values used in Eq. (1), with \prime denoting postshock conditions.

	w_0 (mm)	w'_0 (mm)	Δv (m/s)	k (mm $^{-1}$)	t_0 (μ s)	Γ (mm $^2/\mu$ s)	A	A'
Mach 1.2	3.26	2.47	97.4	1.795	28	0.046	0.67	0.74
Mach 1.5	3.26	1.69	226.4	1.795	15	0.070	0.67	0.79

to be the streamwise location at which the signal rises above the background noise level by at least 40%, and corresponds to about 10% of the peak intensity for a given image. A previous study by Balakumar *et al.*²⁵ with the same experimental setup has utilized quantitative PLIF to determine that this threshold edge intensity corresponds to about 5% SF₆ concentration. This should be a reasonable estimate for one wishing to compare this experimental data with simulations. If a spike or late time remnants of a spike (diffuse opposite facing mushroom) were evident in an image, they were not included in the width measurement, as such small scale features are not accounted for in the mixing width model. The error in all width measurements was determined to be $\pm 3\%$ by varying the threshold value and calculating the resulting changes in the width measurements. At most times, where applicable, the total spread in data, derived from shot to shot variations, was between 3% and 8% of the average width at that time.

Figure 12 shows the mixing width evolution with time for both the Mach 1.2 and 1.5 experiments, along with best fit curves to each data set derived from the Jacobs *et al.* mixing width model described above. In the curve fits, the virtual origin, t_0 was allowed to vary between 0 and 55 μ s for Mach 1.2, and 0 and 20 μ s for Mach 1.5, based upon the observed flow development. The circulation, Γ , was allowed to vary freely. The images in both Mach number experiments at $t=15 \mu$ s in Fig. 7 capture the flow just after shock passage; therefore, the initial width, w'_0 from Eq. (1), was measured experimentally to be $w'_0=2.47$ mm for Mach 1.2, and $w'_0=1.69$ mm for Mach 1.5. The wave number, k , was also

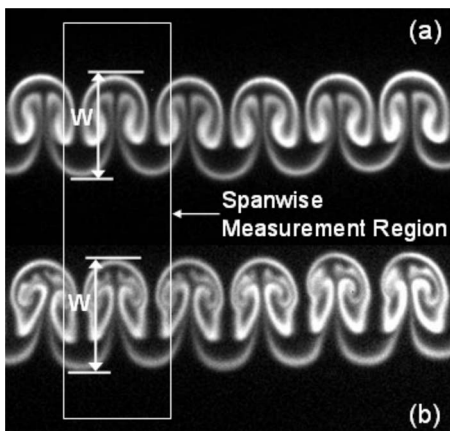


FIG. 11. Integral width measurement, w , for images from two separate runs of the Mach 1.2 experiment. The box indicates the spanwise region of the image that was considered during the measurement process. (a) $t=465 \mu$ s; (b) $t=565 \mu$ s.

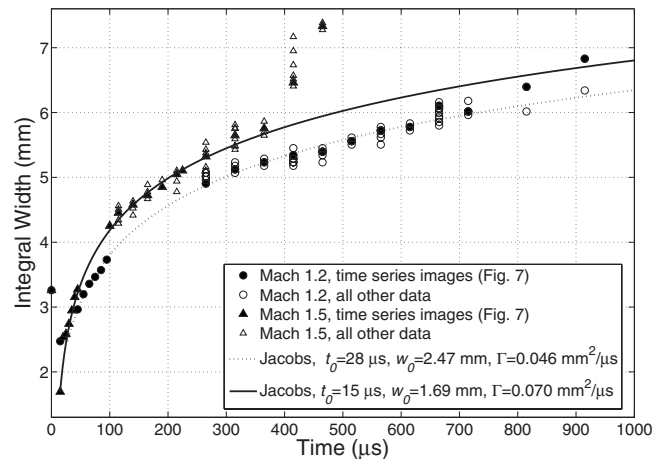


FIG. 12. Integral width vs time; Mach 1.2 vs Mach 1.5. The line curves show theoretical width according to the width model discussed in the text: $\Gamma=0.046$ mm $^2/\mu$ s for Mach 1.2, $\Gamma=0.070$ mm $^2/\mu$ s for Mach 1.5. Data points used to create the time series are delineated.

measured at the imaging plane and fixed at 1.795 mm $^{-1}$. The model curves, with $\Gamma=0.046$ mm $^2/\mu$ s for Mach 1.2, and $\Gamma=0.070$ mm $^2/\mu$ s for Mach 1.5, agree very well with the experimental data until late times when the experimental widths grow faster than those of the model. This behavior appears to have begun by 815 μ s for Mach 1.2, and occurs prominently at 415 μ s for Mach 1.5. Late time disagreement is likely due to a combination of physical departures from the model including the bloblike (as opposed to point) nature of the vortices, the three dimensionality of the flow, and viscous effects. Specifically, the disagreement appears to be the result of the features labeled 3 and 4 in Fig. 7. The fidelity with which this point-vortex model is able to capture the shape of the growth throughout early and intermediate times suggests that the physics in the model is appropriate, in that the flow is vortex dominated. Further experiments allowing velocity measurements, and thus circulation estimates, will be needed to determine whether this model, or variations of this model, have predictive capability.

We expect the width growth rate to have dependence upon the velocity jump (Δv) imparted on the interface because the initial conditions in the current study are related to the classical single interface problem. Richtmyer's formula ($da/dt=kA\Delta va_0$, where A is the Atwood number) gives the growth of perturbation amplitude, a , of a single interface within the linear regime of the instability. In the current experiment, we measure the growth of integral width, w , which is dependent upon the growth of the perturbations on both sides of the fluid layer. In the limit of a thick curtain with no interaction between the two interfaces, one would expect $dw/dt=2da/dt$, based on Richtmyer's formula using pre-shock values. With this motivation, we normalize the time scale by introducing the nondimensional time $\tau=2kA\Delta vt$, where $A=0.67$ is the preshock value. As seen in Fig. 13, the integral width growth rates for the two Mach numbers collapse when integral width is plotted against τ , with a small vertical offset, Δb , separating the widths for the two data sets. While the collapse of the growth rates using this scaling would be expected for a thick curtain within the linear re-

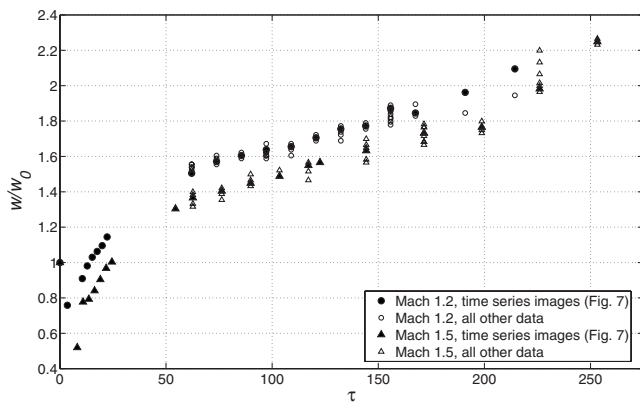


FIG. 13. Nondimensional integral width vs τ , where $w_0=3.26$ mm; Mach 1.2 vs Mach 1.5. Data points used to create the time series are delineated.

gime of the instability, we find that this scaling is effective for the current *thin* gas layer throughout its entire observable evolution, despite strong interaction between the two interfaces.

The offset, $\Delta b=0.166$ is likely due to the difference in compression of the initial conditions by different strength shocks, $\Delta w'_0/w_0=0.239$, measured in the current experiment. However, scaling the vertical axis using this difference in initial condition compression overcompensates for the observed offset, Δb . Therefore, to clearly demonstrate the growth rate collapse when using the nondimensional scaling, we add Δb to the Mach 1.5 widths, as shown in Fig. 14. For clarity, only images used in the time series in Fig. 7 are plotted in Fig. 14. The same scaling and offset was applied to the Jacobs model, also shown in Fig. 14. This result further illustrates that the model captures the large scale mixing trends, and that the nondimensional growth rate is independent of the Mach number in the range studied. More experiments at varying Mach numbers are required to determine (1) whether using convection velocity for the time axis normalization is sufficient for collapse of integral width growth rate for a wide range of Mach number experiments, given the initial conditions in the current study, and (2) if there is a

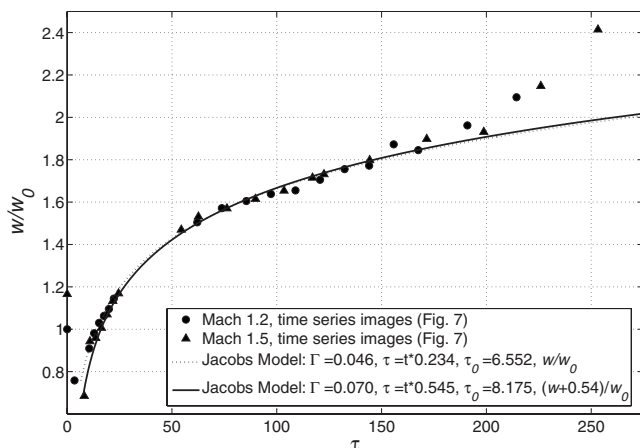


FIG. 14. Nondimensional integral width vs τ , with the offset, $\Delta b=0.166$, added to the Mach 1.5 data. For clarity of presentation, only the images used in the time series are displayed. Lines represent the scaled Jacobs mixing width model.

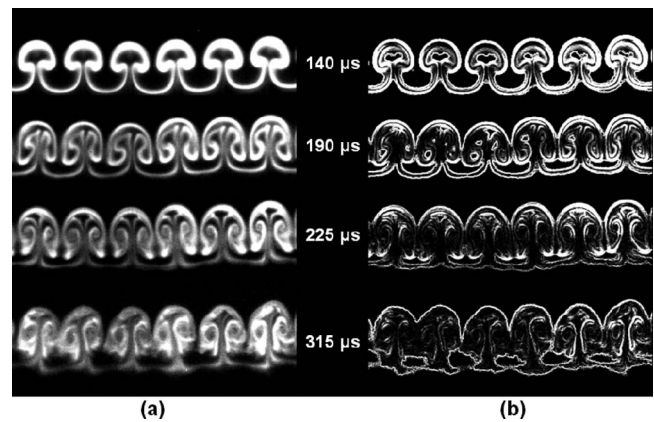


FIG. 15. (a) PLIF intensity maps for four times within the Mach 1.5 experiment; (b) the corresponding maps of instantaneous mixing rate, χ .

consistent algorithm for scaling the integral width axis based perhaps upon some percentage of the difference in compression widths.

C. Instantaneous mixing rate

Integral mixing width is a commonly used metric for quantifying RM flows on the largest scale, and it is useful as a first step for quantitatively comparing mixing between different experiments, and between experiments and models. However, integral mixing width does not capture the details of the mixing on the fine scales. As discussed earlier, a qualitative inspection of Fig. 7 shows differences in the overall flow morphology between Mach 1.2 and 1.5 experiments. Yet, these differences are not readily apparent when comparing the integral width curves (especially when the curves are collapsed as in Fig. 14). To delve further into the fluid physics requires the use of other metrics that quantify mixing processes at smaller scales. In a recent paper, Tomkins *et al.*³⁴ estimated the instantaneous mixing rate, $\chi(x,y,t) \equiv D(\nabla c \cdot \nabla c)$, from quantitative concentration fields, $c(x,y,t)$, for the first time in shock accelerated flows. Here, D is the molecular diffusivity between gases, estimated to be $D=0.98 \times 10^{-5}$ m²/s for air-SF₆, and x and y are the stream-wise and spanwise positions, respectively, within an image. The mixing rate appears as a sink term in an expression for evolution of the scalar “energy” c^2 , and thus χ is a measure of the instantaneous reduction rate of scalar fluctuations in the field.

It should be noted that the PLIF images in the present study are not calibrated concentration field maps, but rather maps of pixel intensity. Therefore, the measurements of χ presented here do not correspond to absolute mixing rates. However, as intensity is proportional to concentration, they do provide the relative change in the instantaneous mixing rate as the flow evolves.

Figure 15 shows both the PLIF images and the corresponding maps of χ for four different times in the Mach 1.5 experiments. A visual inspection shows that at early times, the concentration gradients (intensity gradients) are steepest as the primary instability strains and stretches the SF₆. As time progresses, the regions associated with the vortex

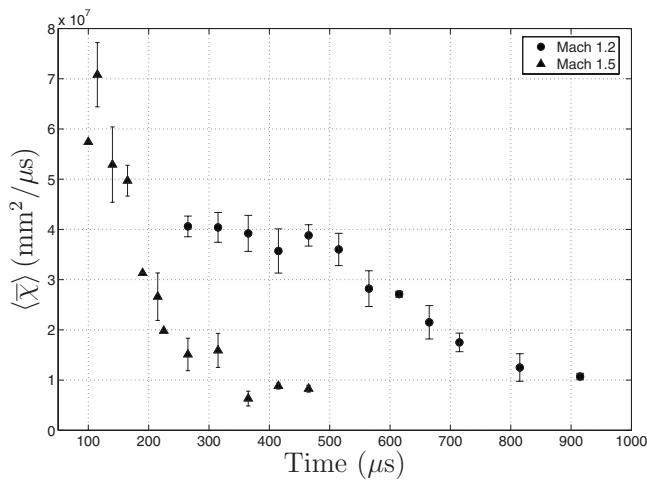


FIG. 16. $\langle \bar{\chi} \rangle$ vs time for Mach 1.2 and 1.5. Error bars represent statistical variation of ± 1 standard deviation.

cores contribute less and less to the instantaneous mixing rate as the material there has already undergone some mixing and concentration gradients are relatively low. Spatially integrating over the map of χ allows for the computation of the total diffusion-driven mixing rate, $\bar{\chi}$, in each image. Averaging over all realizations for a given time then gives $\langle \bar{\chi} \rangle = (\sum_{i=1}^n \iint \chi_i dx dy) / n$, where n is the number of images at a given time. $\langle \bar{\chi} \rangle$ is plotted as a function of time in Fig. 16 for both Mach number experiments for all times that were captured by the dynamic camera.

In general, over the times investigated, $\langle \bar{\chi} \rangle$ decreases with time for both Mach numbers. At early times, material lines are distinct, and straining (due to the vorticity) causes a dramatic increase in both surface area and gradient steepening along that surface area, leading to high values of $\bar{\chi}$. As the instability grows and small scale velocity fluctuations add to the mixing, the structure becomes more mixed, resulting in less intense concentration gradients, and hence reduced instantaneous mixing rates.

We find that the maximum value for $\langle \bar{\chi} \rangle$ over the times observed was nearly twice as high for Mach 1.5 (occurring at $t = 115 \mu\text{s}$) as that for Mach 1.2 (occurring at $t = 265 \mu\text{s}$). Thus, Mach number has a clear effect on the concentration gradients and the instantaneous mixing rate in the flow. These gradients reflect the strength of the deposited vorticity, which strains the concentration layers, suggesting that the vortices in the $M = 1.5$ flow are stronger, as one would expect. Because mixing occurs much faster in the Mach 1.5 case, $\langle \bar{\chi} \rangle$ falls off much more rapidly than in the Mach 1.2 experiments.

$\langle \bar{\chi} \rangle$ is plotted against τ in Fig. 17, using the same time scaling as in Fig. 14. As shown in Fig. 17, the scaling that worked to collapse integral widths does not collapse the $\langle \bar{\chi} \rangle$ data. The failure of this scaling for $\langle \bar{\chi} \rangle$ data collapse is further evidence that integral mixing width is not sufficient if one wants to fully describe the physics governing the flow and understand the mechanisms that drive fluid mixing. Moreover, while useful, integral width measurements should

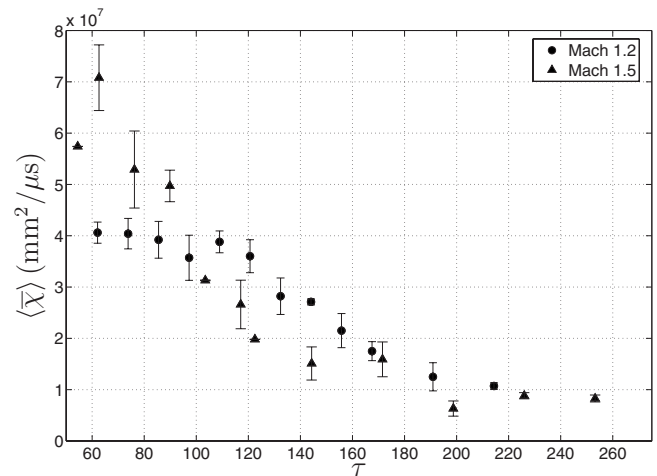


FIG. 17. $\langle \bar{\chi} \rangle$ vs τ for Mach 1.2 and 1.5. Error bars represent statistical variation of ± 1 standard deviation.

not stand alone when one is attempting to make comprehensive comparisons between experiments or models in flows of this nature.

IV. CONCLUSIONS

Experimental results are reported characterizing the Richtmyer–Meshkov instability of a varicose perturbed, heavy-gas curtain after it is impulsively accelerated by shock waves of varying Mach numbers. Qualitative PLIF was used to obtain maps of SF_6 concentration before shock impact and at various times thereafter. The initial conditions were controlled very carefully, resulting in a highly repeatable experiment. Therefore, it is assumed that the differences between the two experiments in large scale flow features are attributable to Mach number effects, which result from differences in (1) the amount of compression of the initial conditions during shock passage, (2) the amount of vorticity deposited, and (3) the refraction of the incident shock front as it passes through the curtain, and the resulting internal reflections of shock waves and expansion waves off each interface.

A time series of 20 PLIF images was constructed for both the Mach 1.2 and the Mach 1.5 data, allowing for qualitative comparison of the postshock flow evolution in each case. Although the large scale flow morphology is similar at early to intermediate times, several qualitative flow features are identified that are considered to be the result of Mach number effect. At later times, these differences become more pronounced and lead to large scale disparities.

A plot of mixing width versus time is presented, showing that growth rate is higher in Mach 1.5 experiments than in those of Mach 1.2. Best fit curves generated using the Jacobs *et al.*¹⁹ mixing width model showed good agreement to the experimental data until late times ($\approx 815 \mu\text{s}$ for Mach 1.2, and $\approx 415 \mu\text{s}$ for Mach 1.5), suggesting that the vortex-dominated physics in the model is appropriate for the present flow at early through intermediate times.

When integral mixing width is plotted against the non-dimensional time scaling, τ , the growth rate is the same for both Mach 1.2 and 1.5 experiments. It is found that two

parameters are needed for collapse of the integral mixing width data: the convection velocity imparted upon the curtain by the incident shock wave, and a fraction of the difference in widths of the postshock, compressed initial conditions.

Measurements of the diffusion driven instantaneous mixing rate, χ , show differences between the two Mach number experiments, even when plotted with the same time scaling used to collapse integral width growth rate. The Mach 1.5 experiments demonstrate much higher maximum instantaneous total mixing rate, $\langle \bar{\chi} \rangle$. $\langle \bar{\chi} \rangle$ then reduces more rapidly for Mach 1.5, as the higher maximum mixing rate subsequently results in a flow with less unmixed fluid. Thus, the use of mixing widths to characterize the flow is an incomplete measure, and other metrics, such as the mixing rate parameter, χ , are useful to describe the flow more fully.

ACKNOWLEDGMENTS

This work was supported by the Department of Energy under Contract No. DE-AC52-06NA25396.

- ¹R. D. Richtmyer, "Taylor instability in shock acceleration of compressible fluids," *Commun. Pure Appl. Math.* **13**, 297 (1960).
- ²Y. Y. Meshkov, "Instability of a shock wave accelerated interface between two gases," NASA Technical Translation No. NASA TT F-13074, 1970.
- ³L. Rayleigh, *The Scientific Papers of Lord Rayleigh* (Cambridge University Press, Cambridge, England, 1900), Vol. 2.
- ⁴G. Taylor, "The instability of liquid surfaces when accelerated in a direction perpendicular to their planes," *Proc. R. Soc. London, Ser. A* **201**, 192 (1950).
- ⁵M. Brouillette, "The Richtmyer-Meshkov instability," *Annu. Rev. Fluid Mech.* **34**, 445 (2002).
- ⁶J. Lindl, "Development of the indirect-drive approach to inertial confinement fusion and the target physics basis for ignition and gain," *Phys. Plasmas* **2**, 3933 (1995).
- ⁷J. Yang, T. Kubota, and E. E. Zukoski, "Applications of shock-induced mixing to supersonic combustion," *AIAA J.* **31**, 854 (1993).
- ⁸G. H. Markstein, "Flow disturbances induced near a slightly wavy contact surface, or flame front, traversed by a shock wave," *J. Aerosp. Sci.* **24**, 238 (1957).
- ⁹W. D. Arnett, J. N. Bahcall, R. P. Kirshner, and S. E. Woosley, "Supernova 1987A," *Annu. Rev. Astron. Astrophys.* **27**, 629 (1989).
- ¹⁰D. Ranjan, M. Anderson, J. Oakley, and R. Bonazza, "Experimental investigation of a strongly shocked gas bubble," *Phys. Rev. Lett.* **94**, 184507 (2005).
- ¹¹D. Ranjan, J. Niederhaus, B. Motl, M. Anderson, J. Oakley, and R. Bonazza, "Experimental investigation of primary and secondary features in high-Mach-number shock-bubble interaction," *Phys. Rev. Lett.* **98**, 024502 (2007).
- ¹²D. Ranjan, J. Niederhaus, J. Oakley, M. Anderson, R. Bonazza, and J. Greenough, "Shock-bubble interactions: Features of divergent shock-refraction geometry observed in experiments and simulations," *Phys. Fluids* **20**, 036101 (2008).
- ¹³J. Jacobs, "The dynamics of shock accelerated light and heavy gas cylinders," *Phys. Fluids A* **5**, 2239 (1993).
- ¹⁴C. D. Tomkins, K. P. Prestridge, P. M. Rightley, P. V. Vorobieff, and R. F. Benjamin, "Flow morphologies of two shock-accelerated, unstable gas cylinders," *J. Visualization* **5**, 273 (2002).
- ¹⁵C. Tomkins, K. Prestridge, P. Rightley, M. Marr-Lyon, P. Vorobieff, and R. Benjamin, "A quantitative study of the interaction of two Richtmyer-Meshkov-unstable gas cylinders," *Phys. Fluids* **15**, 986 (2003).
- ¹⁶D. A. Holder, A. V. Smith, C. J. Barton, and D. L. Youngs, "Shock-tube experiments on Richtmyer-Meshkov instability growth using an enlarged double-bump perturbation," *Laser Part. Beams* **21**, 411 (2003).
- ¹⁷J. W. Jacobs, D. L. Klein, D. G. Jenkins, and R. F. Benjamin, "Instability growth patterns of a shock-accelerated thin fluid layer," *Phys. Rev. Lett.* **70**, 583 (1993).
- ¹⁸J. M. Budzinski, R. F. Benjamin, and J. W. Jacobs, "Influence of initial conditions on the flow patterns of a shock-accelerated thin fluid layer," *Phys. Fluids* **6**, 3510 (1994).
- ¹⁹J. Jacobs, D. Jenkins, D. Klein, and R. Benjamin, "Nonlinear growth of the shock-accelerated instability of a thin fluid layer," *J. Fluid Mech.* **295**, 23 (1995).
- ²⁰P. M. Rightley, P. Vorobieff, and R. F. Benjamin, "Evolution of a shock-accelerated thin fluid layer," *Phys. Fluids* **9**, 1770 (1997).
- ²¹P. M. Rightley, P. Vorobieff, R. Martin, and R. F. Benjamin, "Experimental observations of the mixing transition in a shock-accelerated gas curtain," *Phys. Fluids* **11**, 186 (1999).
- ²²K. Prestridge, P. M. Rightley, P. Vorobieff, R. F. Benjamin, and N. A. Kurnit, "Simultaneous density-field visualization and PIV of a shock-accelerated gas curtain," *Exp. Fluids* **29**, 339 (2000).
- ²³K. Prestridge, P. Vorobieff, P. M. Rightley, and R. F. Benjamin, "Validation of an instability growth model using particle image velocimetry measurements," *Phys. Rev. Lett.* **84**, 4353 (2000).
- ²⁴P. Vorobieff, P. M. Rightley, and R. F. Benjamin, "Shock-driven gas curtain: Fractal dimension evolution in transition to turbulence," *Physica D* **133**, 469 (1999).
- ²⁵B. J. Balakumar, G. C. Orlicz, C. D. Tomkins, and K. P. Prestridge, "Simultaneous particle-image velocimetry-planar laser-induced fluorescence measurements of Richtmyer-Meshkov instability growth in a gas curtain with and without reshock," *Phys. Fluids* **20**, 124103 (2008).
- ²⁶S. Kumar, G. Orlicz, C. Tomkins, C. Goodenough, K. Prestridge, P. Vorobieff, and R. Benjamin, "Stretching of material lines in shock-accelerated gaseous flows," *Phys. Fluids* **17**, 082107 (2005).
- ²⁷T. C. Sangster, R. Betti, R. S. Craxton, J. A. Delettrez, D. H. Edgell, L. M. Elasky, V. Y. Glebov, V. N. Goncharov, D. R. Harding, D. Jacobs-Perkins, R. Janezic, R. L. Keck, J. P. Knauer, S. J. Loucks, L. D. Lund, F. J. Marshall, R. L. McCrory, P. W. McKenty, D. D. Meyerhofer, P. B. Radha, S. P. Regan, W. Seka, W. T. Shmayda, S. Skupsky, V. A. Smalyuk, J. M. Soures, C. Stoeckl, and B. Yaakobi, "Cryogenic DT and D₂ targets for inertial confinement fusion," *Phys. Plasmas* **14**, 058101 (2007).
- ²⁸D. C. Wilson, P. A. Bradley, N. M. Hoffman, F. J. Swenson, D. P. Smitherman, R. E. Chrien, R. W. Margevicius, D. J. Thoma, L. R. Foreman, J. K. Hoffer, S. R. Goldman, S. E. Caldwell, T. R. Dittrich, S. W. Haan, M. M. Marinak, S. M. Pollaine, and J. J. Sanchez, "The development and advantages of beryllium capsules for the National Ignition Facility," *Phys. Plasmas* **5**, 1953 (1998).
- ²⁹K. O. Mikaelian, "Numerical simulations of Richtmyer-Meshkov instabilities in finite-thickness fluids layers," *Phys. Fluids* **8**, 1269 (1996).
- ³⁰G. Orlicz, "Shock driven instabilities in a varicose, heavy-gas curtain: Mach number effects," M.S. thesis, University of New Mexico, 2007.
- ³¹J. W. Jacobs and V. V. Krivets, "Experiments on the late-time development of single-mode Richtmyer-Meshkov instability," *Phys. Fluids* **17**, 034105 (2005).
- ³²R. L. Holmes, G. Dimonte, B. Fryxell, M. L. Gittings, J. W. Grove, M. Schneider, D. H. Sharp, A. L. Velikovich, R. P. Weaver, and Q. Zhang, "Richtmyer-Meshkov instability growth: Experiment, simulation and theory," *J. Fluid Mech.* **389**, 55 (1999).
- ³³B. D. Collins and J. W. Jacobs, "PLIF flow visualization and measurements of the Richtmyer-Meshkov instability of an air/SF₆ interface," *J. Fluid Mech.* **464**, 113 (2002).
- ³⁴C. Tomkins, S. Kumar, G. Orlicz, and K. Prestridge, "An experimental investigation of mixing mechanisms in shock-accelerated flow," *J. Fluid Mech.* **611**, 131 (2008).